Indirect Force Control of a Cable-suspended Aerial Multi-Robot Manipulator

D. Sanalitro[1], M. Tognon[2], A.E. Jimenez Cano[1], J. Cortés[1], A. Franchi[3,1]

Abstract—**We present the control in physical interaction with the environment of a Cable-suspended Aerial Multi-Robot Manipulator (CS-AMRM) called the *Fly-Crane*, composed of three aerial vehicles towed to a platform by means of six cables. The control strategy enables the system to accurately and safely perform tasks involving expected or unexpected interactions between the platform and the environment, in the absence of dedicated force/torque sensors. A previously developed Inverse Kinematic Controller (IKC) is enhanced with an admittance framework, and contacts are estimated through a generalized momentum-based observer. To assess the validity of our approach, and to provide practical insights into the method, we perform extensive experimental tests, comprehending the admittance property shaping to modulate stiffness, damping, and virtual mass, as well as experiments in a more realistic scenario involving contacts between the *Fly-Crane* and the environment.**

Index Terms—**Aerial Systems: Mechanics and Control, Multi-Robot Systems, Compliance and Impedance Control**

I. INTRODUCTION

UAVs have shown their interest to perform various tasks, mostly for contact-less applications such as monitoring and mapping, but recently, also for physical interactions with the environment or with humans [1]. Indeed, possible applications requiring physical contact are numerous: structure assembly, contact-based inspection, transportation, harvesting, etc. The most frequent approach to enable a UAV with manipulation capabilities is based on the installation of dedicated equipment such as grippers or robotic arms [1]. Alternatively, the manipulation/transportation of objects can be performed using cables [2] or tethers [3]. Such a setting has the advantage of simplicity. Nevertheless, stabilizing the oscillation of suspended objects can be difficult, and may imply a significant loss of accuracy. In general, the use of two or more UAVs cooperatively allows better control of the load and larger payload overall. Note however that, systems composed of multiple vehicles rigidly attached to the load [4], as well as systems with multiple robots attached through an insufficient number of cables [5] cannot control the full pose (position and orientation) of the load. Conversely, it has been demonstrated

that a system with three robots, connected to three non-collinear points by means of six cables can achieve such a task if one employs *statically-rigid* designs [6]. One of these systems, called the *Fly-Crane*, was first presented in [7]. Subsequently, a robust controller and a method for the inertial parameters estimation of such a system were introduced in [8] and [9], respectively.

To the best of our knowledge, none of the previous work on Cable-Based Aerial Multi-Robot Manipulators (CS-AMRMs) has provided a controller that can be safely used when the load is in contact with the environment. With this work, we fill such a gap by presenting a method for the interaction control of the *Fly-Crane* system with the surrounding environment and possibly also with humans. In the literature, three classes of interactions can be identified:

1) *Unexpected-collision interactions*: the transportation or the manipulation of objects in adverse circumstances may arise in unexpected collisions that have to be carefully managed.
2) *Expected-collision interactions*: situations where it is known in advance that contacts will take place. As a consequence, such interactions have to be carefully regulated. Examples are: pick-and-place operations, inspection by contact, or peg-in-hole tasks.
3) *Active interactions*: the transportation or the manipulation can be reinforced through direct collaboration with an active external agent such as another robot or a human.

In the aerial robotics domain, one of the critical issues for robot interactions is the measurement/estimation of the interaction wrench[4]. A reliable solution proposed for single-UAV manipulators [11] is to make use of force/torque sensors to measure the interaction forces. However, the costs and weight of such devices cannot be considered negligible for aerial platforms. Moreover, a force/torque sensor can only measure the interaction punctually, where it is mounted, while collisions can occur at any point of the platform. Therefore, alternative solutions based on wrench estimation have to be investigated. In [12], the authors showed a contact force control for an aerial manipulator where the UAV acts as the sensor of the exerted force on the environment. In [13], an IMU-enhanced momentum-based observer was presented. Conversely, in the context of multi-robot systems where the cooperative manipulation has been largely investigated [1], wrench estimators have mainly been employed in evaluating the role of the internal forces in co-manipulation tasks, as

[1]LAAS-CNRS, Université de Toulouse, CNRS, Toulouse, France. dario.sanalitro@laas.fr, antonio-enrique.jimenez-cano@laas.fr juan.cortes@laas.fr antonio.franchi@laas.fr

[2]Autonomous Systems Lab, Department of Mechanical and Process Engineering, ETH Zurich, 8092 Zürich, Switzerland, mtognon@ethz.ch. The author partially contributed while he was at LAAS-CNRS, Toulouse, France

[3]Robotics and Mechatronics lab, Faculty of Electrical Engineering, Mathematics & Computer Science, University of Twente, Enschede, The Netherlands a.franchi@utwente.nl

[4]An interesting framework for collision management for robotic manipulators was introduced in [10]

in [14] while, to the best of our knowledge, wrench estimators have never been employed in the identification of possible external forces/torques acting on a CS-AMRM.

After the identification phase, the aerial multi-robot system has to properly react according to the forces resulting from an interaction event. Only a few works have considered this aspect. In [15], the authors firstly investigated the problem of cooperatively controlling the six DoFs (Degrees-of-freedom) of a flexible platform rigidly attached to three quadrotors by means of three movable bars. In addition, they proved its efficacy in rejecting external disturbances, also showing an example of object telemanipulation. Nevertheless, the authors' main focus was the analysis of the effectiveness of the compliant properties of the system. Therefore, intensity and directional information of the external disturbances, as well as a deeper characterization of the compliant behavior were not entirely described.

In this paper, we show that a well-thought-out selection of methods together with a careful implementation, allows us to solve the aforementioned problems for the control of a CS-AMRM, the *Fly-Crane*, while physically interacting with the environment. Although the employed algorithms are well known in the robotics community, they were mainly conceived for ground manipulators. They have rarely been implemented and evaluated on aerial multi-robot manipulators, and, to the best of our knowledge, never with CS-AMRMs. More precisely, for the first time: *i)* we investigate the reliability of an external wrench estimation method for the control of a CS-AMRM; *ii)* we integrate a 6D impedance shaping algorithm within the control architecture of such a complex system. Moreover, the performance of the proposed approach is evaluated through a set of experiments illustrating the system in one of the three different classes of interactions mentioned above: unexpected collisions. In fact, these are the most common type of interactions that can occur in the envisioned applications of the CS-AMRM under exam.

The paper is organized as follows: Section II introduces the *Fly-Crane* system and its modeling. The control architecture is detailed in Section III. The experimental results are described in Section IV, and Section V presents conclusions and future works.

II. SYSTEM MODELING

The *Fly-Crane* is an aerial manipulator that consists of three aerial vehicles attached to a platform by six cables, two per robot. With this configuration, the robots can exert a 6D wrench to the platform, allowing for 6D motions. The dynamic model has been presented in [9]. For the sake of completeness, here we provide a brief summary. We provide a schematic description of the *Fly-Crane* in Fig. 1. Let us define an inertial frame $\mathcal{F}_W = \{O_W, \boldsymbol{x}_W, \boldsymbol{y}_W, \boldsymbol{z}_W\}$, a body frame $\mathcal{F}_{Ri} = \{O_{Ri}, \boldsymbol{x}_{Ri}, \boldsymbol{y}_{Ri}, \boldsymbol{z}_{Ri}\}$ rigidly attached to the center of i-th robot, and a body frame $\mathcal{F}_P = \{O_P, \boldsymbol{x}_P, \boldsymbol{y}_P, \boldsymbol{z}_P\}$ rigidly attached to the platform, where $O_\star$ and $\{\boldsymbol{x}_\star, \boldsymbol{y}_\star, \boldsymbol{z}_\star\}$ are the origin and unit axes of $\mathcal{F}_\star$. $\mathcal{F}_P$ is placed such that O_P is in the geometric center of the platform. The vector $^W\boldsymbol{p}_P \in \mathbb{R}^3$ describes the position of O_P with respect to $\mathcal{F}_W$
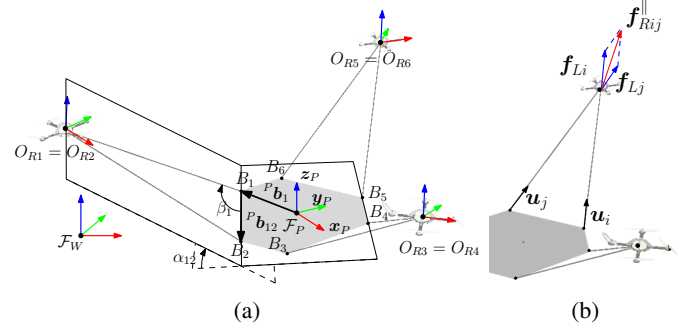

Fig. 1: Schematic representations of the *Fly-Crane* system: (a) shows the relevant variables of the system; (b) shows the forces exerted by each quadrotor and projected on each pair of cables.

and $^W\boldsymbol{R}_P \in SO(3)$ describes the orientation of $\mathcal{F}_P$ with respect to $\mathcal{F}_W$[1]. Applying the Newton-Euler formalism, the dynamics of the platform can be written as

$$
\begin{aligned}
m_P \ddot{\boldsymbol{p}}_P &= -m_P g \boldsymbol{z}_W + \boldsymbol{f}_P + \boldsymbol{f}_e \\
\dot{\boldsymbol{R}}_P &= \boldsymbol{S}(^P\boldsymbol{\omega}_P)\boldsymbol{R}_P \\
\boldsymbol{J}_P {}^P\dot{\boldsymbol{\omega}}_P &= -\boldsymbol{S}(^P\boldsymbol{\omega}_P)\boldsymbol{J}_P {}^P\boldsymbol{\omega}_P + {}^P\boldsymbol{\tau}_P + {}^P\boldsymbol{\tau}_e,
\end{aligned}
\tag{1}
$$

where $m_P \in \mathbb{R}_{>0}$ is the mass of the platform, $g \in \mathbb{R}_{>0}$ is the free-fall acceleration, $\boldsymbol{f}_P, {}^P\boldsymbol{\tau}_P \in \mathbb{R}^3$, are the forces and moments acting on the platform as a consequence of the pulling action of the robots, $\boldsymbol{f}_e$ and $^P\boldsymbol{\tau}_e \in \mathbb{R}^3$ are the external forces and moments perturbing the platform, $\boldsymbol{S}(\star)$ is the skew operator[2], $^P\boldsymbol{\omega}_P \in \mathbb{R}^3$ is the platform angular velocity, and $\boldsymbol{J}_P \in \mathbb{R}^{3\times3}_{>0}$ the inertia of the platform.

As shown in Fig. 1(a), each cable is attached to the platform at point B_i and to an aerial vehicle at point O_{Ri} where $O_{R1} = O_{R2}$, $O_{R3} = O_{R4}$ and $O_{R5} = O_{R6}$. Their position with respect to $\mathcal{F}_W$ is described by the vectors $\boldsymbol{b}_i \in \mathbb{R}^3$ and $\boldsymbol{p}_{Ri} \in \mathbb{R}^3$, respectively. As commonly done, we consider each cable with a constant length, $l_i \in \mathbb{R}_{>0}$ (no elastic deformations), and negligible mass and inertia. Furthermore, we assume no rotational constraints at the anchoring points.

We denote with $f_i \in \mathbb{R}_{\geq0}$ the intensity of the internal force along the i-th cable. Notice that if $f_i > 0$ the cable is taut, while it is slack if $f_i = 0$. The aim is to move the system always preserving the tautness of each cable, such that $f_i > 0$ for all $i = 1, \dots, 6$. The force on each cable can be defined as $\boldsymbol{f}_{Li} = f_i \boldsymbol{n}_i \in \mathbb{R}^3$, where $\boldsymbol{n}_i \in \mathbb{R}^3$ is the unit vector along $\overrightarrow{B_i O_{Ri}}$ which describes the orientation of each cable with respect to $\mathcal{F}_W$. All the forces can be then collected in $\boldsymbol{f} = [\boldsymbol{f}_{L1}^\top, \boldsymbol{f}_{L2}^\top, \dots, \boldsymbol{f}_{L6}^\top]^\top \in \mathbb{R}^{18}$ and can be used in the definition of all the wrenches applied to the platform $\boldsymbol{w}_P = [\boldsymbol{f}_P^\top \ {}^P\boldsymbol{\tau}_P^\top]^\top$ as follows

$$
\boldsymbol{w}_P = \boldsymbol{G}(\boldsymbol{R}_P)\boldsymbol{f},
\tag{2}
$$

where $\boldsymbol{G}$ is a matrix defined as

$$
\boldsymbol{G} = \begin{bmatrix} \boldsymbol{I}_3 & \dots & \boldsymbol{I}_3 \\ \boldsymbol{S}(^P\boldsymbol{b}_1)\boldsymbol{R}_P^\top & \dots & \boldsymbol{S}(^P\boldsymbol{b}_6)\boldsymbol{R}_P^\top \end{bmatrix}.
\tag{3}
$$

[1]The left superscript indicates the reference frame. From now on, $\mathcal{F}_W$ is considered as reference frame when the superscript is omitted.
[2]$\boldsymbol{S}(\star) : \mathbb{R}^3 \to \mathbb{R}^{3\times3}$ is such that $\boldsymbol{S}(\boldsymbol{v})\boldsymbol{u} = \boldsymbol{v} \times \boldsymbol{u} \ \forall \boldsymbol{v}, \boldsymbol{u} \in \mathbb{R}^3$

The thrust generation units of the system are the aerial vehicles attached to the platform by means of the pair of cables (i, j). $\boldsymbol{f}_{Rij} \in \mathbb{R}^3$ is the 3D controllable total thrust vector of each vehicle, after gravity compensation:

$$\boldsymbol{f}_{Rij} = \boldsymbol{R}_{Ri} \begin{bmatrix} 0 \\ 0 \\ \sum_{k=1}^{4} c_f \omega_{ki}^2 \end{bmatrix} - m_{Ri} \boldsymbol{g} \qquad (4)$$

where ω_{ki} is the spinning rate of each propeller of the i-th quadrotor, $c_f \in \mathbb{R}_{>0}$ represents a propeller-dependent constant parameter, $m_{Ri} \in \mathbb{R}_{>0}$ is the mass of each robot and finally $\boldsymbol{g} = [0\ 0\ g]^\top$ is the gravity vector. Assuming that the cables are always taut, it is possible to define a thrust intensity vector which lies on the plane formed by each pair of cables (see Fig. 1(b)), such as

$$\boldsymbol{f}_{Rij}^{\parallel} = \left(\boldsymbol{I}_3 - \boldsymbol{n}_{ij}\boldsymbol{n}_{ij}^\top\right)\boldsymbol{f}_{Rij} = f_i \boldsymbol{n}_i + f_j \boldsymbol{n}_j, \qquad (5)$$

where $\boldsymbol{I}_n \in \mathbb{R}^{n \times n}$ is the identity matrix of dimension n, and $\boldsymbol{n}_{ij}$ is the unit normal vector of the plane generated by $\boldsymbol{n}_i$ and $\boldsymbol{n}_j$ such that

$$\boldsymbol{n}_{ij} = (\boldsymbol{n}_i \times \boldsymbol{n}_j) / \|\boldsymbol{n}_i \times \boldsymbol{n}_j\|. \qquad (6)$$

Finally f_i and f_j are the solutions of the following system

$$\begin{cases} f_i\left(\boldsymbol{n}_i \cdot \boldsymbol{n}_i\right) + f_j\left(\boldsymbol{n}_i \cdot \boldsymbol{n}_j\right) = \boldsymbol{f}_{Rij}^{\parallel} \cdot \boldsymbol{n}_i \\ f_i\left(\boldsymbol{n}_j \cdot \boldsymbol{n}_i\right) + f_j\left(\boldsymbol{n}_j \cdot \boldsymbol{n}_j\right) = \boldsymbol{f}_{Rij}^{\parallel} \cdot \boldsymbol{n}_j \end{cases}. \qquad (7)$$

In the end, the force along each cable pair turns out to be

$$\boldsymbol{f}_{Li} = f_i \boldsymbol{n}_i \quad \boldsymbol{f}_{Lj} = f_j \boldsymbol{n}_j. \qquad (8)$$

The configuration of the pair of cables (i, j) is given by the angle $\alpha_{ij} \in \mathbb{R}$ between the plane where the cables (i, j) lay and the one composed of the axis $\{\boldsymbol{x}_P, \boldsymbol{y}_P\}$. Therefore, the platform configuration can be entirely described by $(\boldsymbol{p}_P, \boldsymbol{R}_P, \boldsymbol{\alpha}) \in \mathcal{C} = SE(3) \times \mathbb{R}^3$, where $\boldsymbol{\alpha} = [\alpha_{12}\ \alpha_{34}\ \alpha_{56}]^\top \in \mathbb{R}^3$. Let us denote with $\boldsymbol{q} = \left[\boldsymbol{p}_P^\top\ \boldsymbol{\eta}_P^\top\ \boldsymbol{\alpha}^\top\right]^\top \in \mathbb{R}^9$ the generalized coordinates of the system, where $\boldsymbol{\eta}_P = [\phi\ \theta\ \psi]^\top \in \mathbb{R}^3$ is an Euler angle parametrization of $\boldsymbol{R}_P$. By direct kinematics, the position of the aerial vehicles $\boldsymbol{p}_{Ri}$, can be computed:

$$\boldsymbol{p}_{Ri}(\boldsymbol{q}) = \boldsymbol{p}_P + \boldsymbol{R}_P\,{}^P\boldsymbol{p}_{Ri}(\alpha_{ij}), \qquad (9)$$

where ${}^P\boldsymbol{p}_{Ri} = {}^P\boldsymbol{b}_i + l_i \boldsymbol{R}_{{}^P\boldsymbol{b}_{ij}}(\alpha_{ij})\boldsymbol{R}_{\boldsymbol{z}_P}(\beta_i)\frac{{}^P\boldsymbol{b}_{ij}}{\|{}^P\boldsymbol{b}_{ij}\|}$, ${}^P\boldsymbol{b}_{ij}$ is the vector $\overrightarrow{B_iB_j}$ expressed in $\mathcal{F}_P$ and $\beta_i \in \mathbb{T}$ is the angle between $\overrightarrow{B_iB_j}$ and $\overrightarrow{B_iO_{Ri}}$. Notice that β_i is a constant of the system that depends on the geometry of the platform and on the length of the cables only. The rotation matrices $\boldsymbol{R}_{{}^P\boldsymbol{b}_{ij}}(\alpha_{ij})$ and $\boldsymbol{R}_{\boldsymbol{z}_P}(\beta_i)$ represent the rotation of α_{ij} about axis ${}^P\boldsymbol{b}_{ij}$ and the rotation of β_i about axis $\boldsymbol{z}_P$, respectively.

Let $\boldsymbol{v}_R = \left[\boldsymbol{v}_{R1}^\top\ \boldsymbol{v}_{R2}^\top\ \boldsymbol{v}_{R3}^\top\right]^\top$ be the velocities of the aerial vehicles. The relation between the system configuration time derivative, $\dot{\boldsymbol{q}}$, and the robot velocities, $\boldsymbol{v}_R$, is defined as:

$$\boldsymbol{v}_R := \dot{\boldsymbol{p}}_R = \boldsymbol{J}(\boldsymbol{q})\dot{\boldsymbol{q}}, \qquad (10)$$

where $\boldsymbol{J} \in \mathbb{R}^{9 \times 9}$ is the Jacobian matrix which describes the mapping between the joint velocities (i.e. the velocities of the

three UAVs) and the corresponding platform linear and angular velocity, $\dot{\boldsymbol{q}} = [\dot{\boldsymbol{p}}_P^\top\ \dot{\boldsymbol{\eta}}_P^\top\ \boldsymbol{\eta}_P^\top]^\top \in \mathbb{R}^9$, and $\boldsymbol{p}_R = [\boldsymbol{p}_{R1}^\top\ \boldsymbol{p}_{R2}^\top\ \boldsymbol{p}_{R3}^\top]^\top$.

The generalized momentum of the platform $\boldsymbol{p} \in \mathbb{R}^6$ is

$$\boldsymbol{p} = \boldsymbol{M}_P(\boldsymbol{q}_P)\dot{\boldsymbol{q}}_P, \qquad (11)$$

where $\boldsymbol{q}_P = [\boldsymbol{p}_P^\top\ \boldsymbol{\eta}_P^\top]^\top$ and $\dot{\boldsymbol{q}}_P = [\dot{\boldsymbol{p}}_P^\top\ \dot{\boldsymbol{\eta}}_P^\top]^\top$ are the configuration of the platform and its derivative. From (1), the time evolution of $\boldsymbol{p}$ can be written as

$$\dot{\boldsymbol{p}} = \boldsymbol{\tau} + \dot{\boldsymbol{M}}_P(\boldsymbol{q}_P)\dot{\boldsymbol{q}}_P - \boldsymbol{C}_P(\boldsymbol{q}_P, \dot{\boldsymbol{q}}_P)\dot{\boldsymbol{q}}_P - \boldsymbol{g}_P(\boldsymbol{q}_P), \quad (12)$$

where $\boldsymbol{\tau} = \boldsymbol{w}_P + \boldsymbol{w}_e \in \mathbb{R}^6$ represents the total wrench applied on the platform and it is the sum of the active force and torques, $\boldsymbol{w}_P \in \mathbb{R}^6$, and the external wrenches, $\boldsymbol{w}_e = [\boldsymbol{f}_e^\top\ {}^P\boldsymbol{\tau}_e^\top]^\top \in \mathbb{R}^6$; $\boldsymbol{C}_P(\boldsymbol{q}_P, \dot{\boldsymbol{q}}_P) \in \mathbb{R}^6$ is the centripetal and Coriolis vector, and $\boldsymbol{g}_P(\boldsymbol{q}_P) \in \mathbb{R}^6$ is the platform gravity vector.

The dynamics of the whole system, composed by the platform and the aerial robots, can be summarized as

$$\boldsymbol{M}(\boldsymbol{q})\ddot{\boldsymbol{q}} + \boldsymbol{C}(\boldsymbol{q}, \dot{\boldsymbol{q}})\dot{\boldsymbol{q}} + \boldsymbol{n}(\boldsymbol{q}) = \boldsymbol{J}^\top(\boldsymbol{q})\left(\begin{bmatrix} \boldsymbol{f}_{R12} \\ \boldsymbol{f}_{R34} \\ \boldsymbol{f}_{R56} \end{bmatrix} + \bar{\boldsymbol{w}}_e \right), \quad (13)$$

where $\boldsymbol{M} \in \mathbb{R}^{9 \times 9}$ is the generalized inertia matrix, $\boldsymbol{C}(\boldsymbol{q}, \dot{\boldsymbol{q}}) \in \mathbb{R}^9$ is the centripetal and Coriolis vector, $\bar{\boldsymbol{w}}_e = [\boldsymbol{w}_e^\top \boldsymbol{0}_3^\top]^\top \in \mathbb{R}^9$ and $\boldsymbol{n}(\boldsymbol{q}) \in \mathbb{R}^9$ is the gravitational effect such as

$$\boldsymbol{n}(\boldsymbol{q}) = m_P \begin{bmatrix} \boldsymbol{g} \\ \boldsymbol{0} \\ \boldsymbol{0} \end{bmatrix} + m_R \boldsymbol{J}(\boldsymbol{q})^\top \begin{bmatrix} \boldsymbol{g} \\ \boldsymbol{g} \\ \boldsymbol{g} \end{bmatrix}, \qquad (14)$$

III. CONTROL

Here we present the proposed control architecture, schematically depicted in Fig. 2. It is composed of three nested loops:

1) The *outer control loop* takes care of the interaction task by generating compliant system trajectories based on the external wrenches acting on the platform;
2) The *intermediate control loop* is a centralized controller that generates the velocity reference for each aerial vehicle, given the desired platform pose. At this level, the redundancy of the *Fly-Crane* with respect to the 6D positioning task is exploited to balance the robot efforts;
3) The *inner control loop* running on each aerial vehicle is a position controller computing the motors' commands given the desired robot trajectory.

A. Intermediate and Inner Control Loop

The *intermediate loop* generates the three aerial vehicles reference velocities $\boldsymbol{v}_R^\star \in \mathbb{R}^9$ to track the desired trajectory for the system configuration $\boldsymbol{q}^d(t)$. For this we rely on a kinematic controller presented in [8]. In particular, given the system desired configuration $\boldsymbol{q}^d = [\boldsymbol{p}_P^{d\,\top}\ \boldsymbol{\eta}_P^{d\,\top}\ \boldsymbol{\alpha}^{d\,\top}]^\top$, the corresponding generalized velocities $\dot{\boldsymbol{q}}^d = [\dot{\boldsymbol{p}}_P^{d\,\top}\ \dot{\boldsymbol{\eta}}_P^{d\,\top}\ \dot{\boldsymbol{\alpha}}^{d\,\top}]^\top$ and the measured configuration $\boldsymbol{q}$, the robot reference velocities can be computed as

$$\boldsymbol{v}_R^\star = \boldsymbol{J}(\boldsymbol{q})(\boldsymbol{K}_{\boldsymbol{q}}\boldsymbol{e}_{\boldsymbol{q}} + \dot{\boldsymbol{q}}^d), \qquad (15)$$
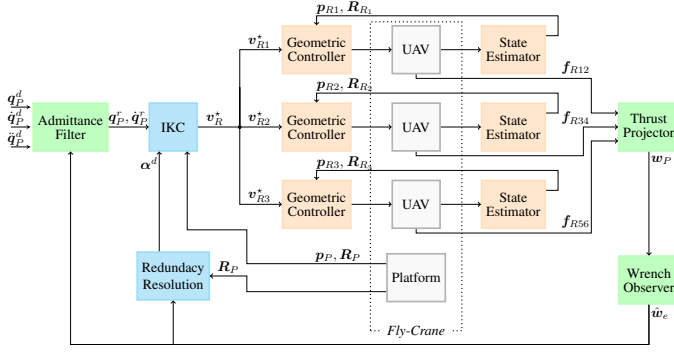
Fig. 2: Control architecture of the admittance framework of the *Fly-Crane* system. The *outer loop* in green, the *intermediate loop* in blue, and the *inner loop* in red.

where $\boldsymbol{K_q} = k_q \boldsymbol{I}_9 \in \mathbb{R}^{9 \times 9}_{>0}$ is a positive definite matrix and $\boldsymbol{e_q} = \boldsymbol{q}^d - \boldsymbol{q}$. Considering the task of controlling the 6D platform pose, the desired angles of the cables, $\boldsymbol{\alpha}^d$, are computed with a local optimizer similar to [9] which allows to resolve the redundancy of the system. The objective is to equally share the effort among the robots, considering the platform weight and the external wrenches acting on it. Moreover, the algorithm allows to maintain the tautness of the cables at a steady-state after a settling phase during the transient.

B. Outer Control Loop: Admittance Framework

An admittance framework, composed of a wrench observer and an admittance filter, allows to handle the physical interaction between the aerial system and the environment. The wrench observer allows to estimate and characterize interaction forces and torques. The admittance filter provides the reference to the intermediate control pool (motion control of the *Fly-Crane*) to be compliant against the interaction wrench.

1) Contact wrench estimation: Interactions, collisions or contacts knowledge is fundamental when a robot moves in cluttered environments. Particularly relevant are the direction and the intensity of the interaction forces. Force-torque sensors could be integrated into the architecture. However, their main limitation of providing only local information makes them not suitable with wide-ranging end-effectors. As a consequence, a monitoring method based on the generalized momentum [10] has been considered such that collision detection and collision identification can be always guaranteed at any platform point, providing sufficiently accurate estimations. Additionally, the generalized momentum method represents a less expensive solution and avoids the need of equipping the aerial manipulator with additional weight.

Following the approach introduced in [16] for robotic manipulators, the momentum observer dynamics derived from (12) is

$$\begin{aligned} \dot{\hat{\boldsymbol{p}}} &= \boldsymbol{w}_P - \boldsymbol{C}_P^\top(\boldsymbol{q}_P, \dot{\boldsymbol{q}}_P)\dot{\boldsymbol{q}}_P - \boldsymbol{g}(\boldsymbol{q}_P) + \hat{\boldsymbol{w}}_e \\ \dot{\hat{\boldsymbol{w}}}_e &= \boldsymbol{K}_O(\dot{\boldsymbol{p}} - \dot{\hat{\boldsymbol{p}}}) \end{aligned}, \quad (16)$$

where the property $\dot{\boldsymbol{M}}_P(\boldsymbol{q}_P) = \boldsymbol{C}_P(\boldsymbol{q}_P, \dot{\boldsymbol{q}}_P) + \boldsymbol{C}_P^\top(\boldsymbol{q}_P, \dot{\boldsymbol{q}}_P)$ has been used and $\boldsymbol{K}_O = diag\{k_O\} > 0 \in \mathbb{R}^{6 \times 6}$ is the diagonal observer gain matrix. For the sake of compactness,

let us write $\boldsymbol{\beta}_P = \boldsymbol{C}_P(\boldsymbol{q}_P, \dot{\boldsymbol{q}}_P)\dot{\boldsymbol{q}}_P + \boldsymbol{g}(\boldsymbol{q}_P)$. The signal $\hat{\boldsymbol{w}}_e(t)$, which represents the estimated external disturbance, is obtained integrating (16) as follow

$$\hat{\boldsymbol{w}}_e = \boldsymbol{K}_O\left(\boldsymbol{p}(t) - \int_{t_0}^t \dot{\boldsymbol{p}}(s)ds - \boldsymbol{p}(0)\right) \quad (17)$$

$$= \boldsymbol{K}_O\left(\boldsymbol{p}(t) - \int_{t_0}^t \left(\boldsymbol{w}_P - \boldsymbol{\beta}_P + \hat{\boldsymbol{w}}_e\right)ds - \boldsymbol{p}(0)\right), \quad (18)$$

where t and t_0 are the current and initial time instant. In ideal conditions, the residual vector $\hat{\boldsymbol{w}}_e$ can be seen as a virtual sensor for external wrenches acting on a rigid body. As a matter of fact, the relation between $\boldsymbol{w}_e$ and $\hat{\boldsymbol{w}}_e$ is

$$\dot{\hat{\boldsymbol{w}}}_e = \boldsymbol{K}_O(\boldsymbol{w}_e - \hat{\boldsymbol{w}}_e), \quad (19)$$

and represents a first-order low-pass filter with the property that $\hat{\boldsymbol{w}}_e \to \boldsymbol{w}_e$ when $t \to \infty$ and $\hat{\boldsymbol{w}}_e \simeq \boldsymbol{w}_e$ when $\boldsymbol{K}_O \simeq \infty$.

2) External wrench compliance: To handle the physical interactions and make the platform of the *Fly-Crane* compliant to interaction wrenches with the environment, we choose the admittance control framework over the impedance one. This choice grounds on the fact that the admittance controller shows better performance for trajectory tracking in free space and disturbance rejection [17].

The admittance framework generates desired motions for the system based on the measured wrench. In our case, given a platform desired trajectory $\boldsymbol{q}_P^d(t) = [\boldsymbol{p}_P^d(t)^\top \ \boldsymbol{\eta}_P^d(t)^\top]^\top$, the admittance filter generates a modified reference trajectory $\boldsymbol{q}_P^r(t)$ based on the effect of the external disturbances $\hat{\boldsymbol{w}}_e$. $\boldsymbol{q}_P^r(t)$ is then provided as reference to the *Fly-Crane* inverse kinematic motion controller. The reference trajectory is computed such that the controlled platform behaves similarly to an admittance model characterized by the following equation

$$\boldsymbol{M}_A(\ddot{\boldsymbol{q}}_P^d - \ddot{\boldsymbol{q}}_P^r) + \boldsymbol{D}_A(\dot{\boldsymbol{q}}_P^d - \dot{\boldsymbol{q}}_P^r) + \boldsymbol{K}_A(\boldsymbol{q}_P^d - \boldsymbol{q}_P^r) = \hat{\boldsymbol{w}}_e, \quad (20)$$

where $\boldsymbol{M}_A = diag\{M_A\} \in \mathbb{R}^{6 \times 6}_{>0}$, $\boldsymbol{D}_A = diag\{D_A\} \in \mathbb{R}^{6 \times 6}_{>0}$ and $\boldsymbol{K}_A = diag\{K_A\} \in \mathbb{R}^{6 \times 6}_{>0}$ are matrices representing the desired (apparent) inertia, damping and stiffness, and

$$\boldsymbol{q}_P^d - \boldsymbol{q}_P^r = \begin{bmatrix} \boldsymbol{p}_P^d - \boldsymbol{p}_P^r \\ \frac{1}{2}\left(\boldsymbol{R}_P^d \boldsymbol{R}_P^{r\top} - \boldsymbol{R}_P^r \boldsymbol{R}_P^{d\top}\right)^\vee \end{bmatrix}. \quad (21)$$

The operator $[\cdot]^\vee$ represents the mapping from $SO(3)$ to $\mathbb{R}^3$. Regarding the stability of the overall system, the bandwidth of the admittance controller has to be lower than the equivalent bandwidth of the inverse kinematic motion control loop [17].

IV. EXPERIMENTS

In this section, we present experimental results that show the effectiveness of the presented control framework. First, we highlight the variety of behaviors that the system is capable of performing changing the physical properties of the admittance filter in Sec. IV-B1. Then we test the multi-robot aerial manipulator system in an *unexpected-collision* scenario, confirming its suitability in executing tasks while being in contact with the environment (see Sec. IV-B2). The interested reader can watch the attached video to see the system in action.
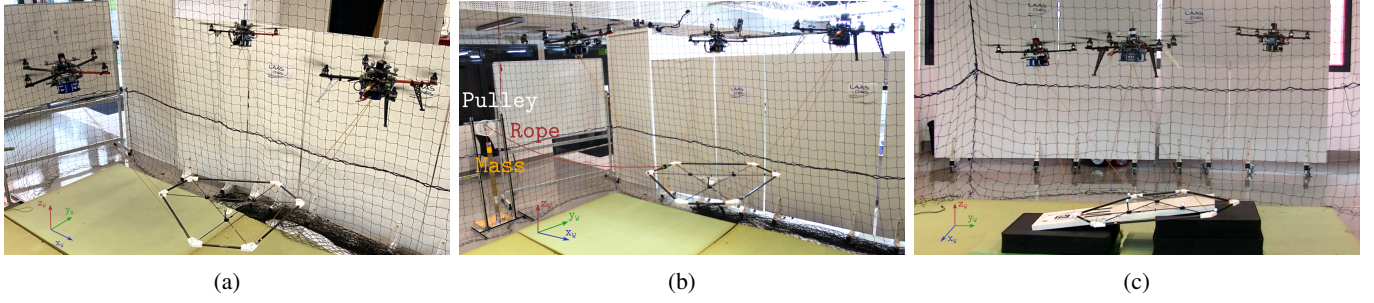
Fig. 3: The *Fly-Crane* involved in three different scenarios: (a) shows the *Fly-Crane* in a contact-free scenario; (b) illustrates the pulley-cable system which has been employed for the admittance property shaping; (c) shows the real-case scenario where the *Fly-Crane* has to approach a tilted surface being compliant with it.

A. Experimental Setup

1) Hardware: The *Fly-Crane* consists of three Quadrotor UAVs connected by six cables to a platform made of carbon fiber bars (see Fig. 3). The platform weights $0.737\,[\mathrm{Kg}]$, each cable length is $1\,[\mathrm{m}]$ and the weight of the aerial vehicles is $1.03\,[\mathrm{Kg}]$ each. The aerial vehicles are equipped with a standard flight controller, four ESCs (Electronic speed controllers) regulating the propeller speed in closed-loop [18], and an onboard PC.

2) Software: The control framework runs partially onboard and partially on a Desktop PC. Each UAV runs onboard its state estimator and position controller [19]. The desktop PC runs a Matlab/Simulink code which implements the inverse kinematics controller, the admittance filter, the wrench observer, and the redundancy resolution. The communication between the desktop PC and the onboard computers passes through a WI-fi connection and runs at $100\,[\mathrm{Hz}]$. The intermediate and inner control loops are then closed based on the estimated state of the vehicles and the platform. The outer loop is closed through the thrust produced by the propellers computed from their measured speed, properly projected along the cables. State estimates are computed onboard at $1\,[\mathrm{kHz}]$ by an UKF (Unscented Kalman filter) that fuses the Motion Capture (Mo-Cap) System measurements (at $120\,[\mathrm{Hz}]$) with the IMU measurements (at $1\,[\mathrm{kHz}]$). Before the start of each experiment, the system goes to a hovering phase reaching a singularity-free configuration, then the admittance framework is activated.

B. Experimental Results

1) Admittance Shaping: This section illustrates the different behaviours of the system obtained by applying a step response when changing the admittance parameters.

In all the experiments, the equilibrium pose for the platform, in absence of external disturbances, is $\boldsymbol{p}_P^d = [0\ 0\ 1.28]^\top\,[\mathrm{m}]$ and $\boldsymbol{R}_P^d = \boldsymbol{I}_3$. Two sets of experiments are presented: *Set-1* (Fig. 4(d)–4(f)) and *Set-2* (Fig. 4(g)–4(i)).

- *Set-1*: at the equilibrium pose and in absence of external force, a constant virtual external force of $f_{n,x} = -1.7\,[\mathrm{N}]$ is suddenly applied along $\boldsymbol{x}_W$, as shown in dashed lines in Fig. 4(a)-4(c).
- *Set-2*: at the equilibrium pose and in absence of external force, a real external force is suddenly applied along $\boldsymbol{x}_W$

using a weight suspended by a pulley-cable system. The reached final force depends only on the weight of the mass,x and it is about -1.7 $[\mathrm{N}]$ (see Fig. 3(b)) for the case under exam. However, the system is unaware of the mass amount, and the force is estimated using the wrench observer described in (19). The behavior through the different experiments is shown in Fig. 4(a)-4(c) in solid lines. In the practical realization, a constant bias in $\hat{\boldsymbol{w}}_e$ has been noticed. We believe that this is caused by modeling errors in the aerial vehicles and platform manufacturing, as well as model uncertainties like rotors and cables models. To mitigate the effect of the bias, a simple calibration is done in order to compensate for the steady-state error at rest.

Testing the system both with a virtual disturbance (perfectly known) and a real force estimated through the wrench observer, let us assess the impact of the wrench observer and other non-modeled effects, such as, e.g., the friction of the pulley, on the entire closed loop architecture.

The three parameters $\boldsymbol{M}_A$, $\boldsymbol{D}_A$, $\boldsymbol{K}_A$, which define the virtual admittance, have been individually manipulated in the different experiments. Additionally, to make further comparisons, we also show the nominal output of an ideal mass-spring-damper system with the same characteristic and subjected to the same external input. As reference values we chose $\boldsymbol{M}_A = 4\boldsymbol{I}_3\,[\mathrm{Kg}]$, $\boldsymbol{D}_A = 10\boldsymbol{I}_3\,[\mathrm{Ns/m}]$, $\boldsymbol{K}_A = 7\boldsymbol{I}_3\,[\mathrm{N/m}]$ and all the other values have been generated by increasing or decreasing such values by suitable deltas. In the first set of comparisons, see Fig. 4(d) and Fig. 4(g), the focus is on the stiffness constant $\boldsymbol{K}_A$. The aim was to evaluate the behavior of the platform at steady-state. For this purpose we selected $\boldsymbol{K}_A = 4\boldsymbol{I}_3\,[\mathrm{N/m}]$, the reference $\boldsymbol{K}_A = 7\boldsymbol{I}_3\,[\mathrm{N/m}]$ and $\boldsymbol{K}_A = 10\boldsymbol{I}_3\,[\mathrm{N/m}]$. The performances of the system, when the external force was both applied (charging phase) and removed (discharging phase), are shown in the graphs in their left and right halves, respectively. The admittance scheme suitably performs at steady-state, where the position of the platform remains close to the nominal one (i.e. $p_{n,x}$) according to the corresponding stiffness value. The maximum error ($e_{P_x} = p_{n,x} - p_{P,x}$) between the nominal position and the actual one does not exceed 0.01 $[\mathrm{m}]$. As expected, three different steady-state positions, -0.1 $[\mathrm{m}]$, -0.2 $[\mathrm{m}]$, -0.4 $[\mathrm{m}]$, have been obtained during the experimental campaign as a

(a): Stiffness tests: virtual and estimated force

(b): Damping tests:virtual and estimated force

(c): Inertia tests: virtual and estimated force

(d): Stiffness tests with perfectly known force: nominal and real position.

(e): Damping tests with perfectly known force: nominal and real velocity.

(f): Inertia tests with perfectly known force: nominal and real acceleration.

(g): Stiffness tests with estimated force: nominal and real position.

(h): Damping tests with estimated force: nominal and real velocity.

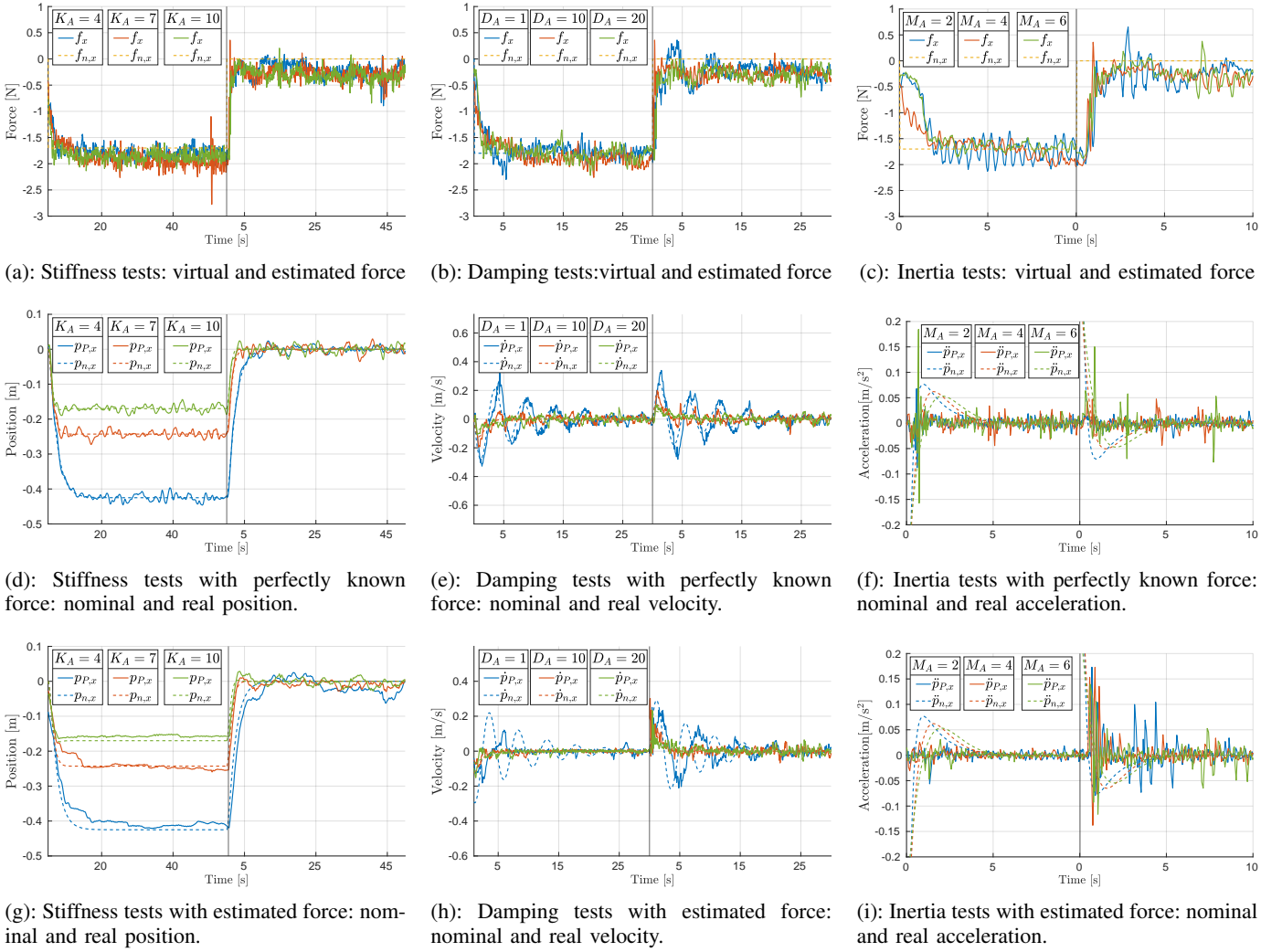(i): Inertia tests with estimated force: nominal and real acceleration.

Fig. 4: Admittance Shaping step responses: The graphs show two phases: on the left of the black line we apply the constant force (charging phase), right after the black line the constant force is removed (discharging phase). Since the force has only been applied along $\boldsymbol{x}_W$, we show the first component of the position/velocity/acceleration vector (solid lines). We make the comparison with the ideal mass-spring-damper system (dashed lines) to underline the admittance shaping capability. In Fig. 4(d) the stiffness $\boldsymbol{K}_A$ has been changed, obtaining three different steady-state positions. On the contrary, in Fig. 4(e) the $\boldsymbol{D}_A$ has been the subject of the variation. Fig. 4(f) shows the effects of changing the virtual mass $\boldsymbol{M}_A$.

consequence of three different stiffness values. On the other side, in the transient of the charging phase of *Set-2* the filtering action of the wrench observer has a non-negligible role in slowing down the reactivity of the system, as it can be seen comparing Fig. 4(g) with Fig. 4(d).

The second set of comparisons (Fig. 4(e) and Fig. 4(h)) shows the effects of the damping constant variation $\boldsymbol{D}_A$. The purpose is to assess the behavior of the platform in the transient phase. The chosen values for the comparison are $\boldsymbol{D}_A = 1\boldsymbol{I}_3$ [Ns/m], the reference $\boldsymbol{D}_A = 10\boldsymbol{I}_3$ [Ns/m], and $\boldsymbol{D}_A = 20\boldsymbol{I}_3$ [Ns/m]. Moreover, the nominal velocity reference $\dot{\boldsymbol{p}}_n$ of the ideal mass-spring-damper system and the actual platform velocity $\dot{\boldsymbol{p}}_P$ have been examined side by side. Two major behaviors can be extrapolated from the observation of the graphs. At first, in *Set-2* (Fig. 4(h)), the ideal mass-spring-damper system is better emulated during the discharging phase rather than the charging one. Unavoidable sticky-slips effects and friction in the pulley-cable significantly affect the natural evolution of the system. As a matter of fact, they do not arise during the discharging phase. Secondly, there is a small tracking delay of $\dot{\boldsymbol{p}}_P$ with respect to $\dot{\boldsymbol{p}}_n$ which is much more accentuated in *Set-2* when $\boldsymbol{D}_A = 1\boldsymbol{I}_3$ [Ns/m]. This latter result is a direct consequence of using the wrench estimator. No differences can be appreciated in the reached steady-state value of the position ($\simeq$-0.2 [m], not shown in the plots), which remains unchanged in all three cases.

In the last experimental tests, Fig. 4(f) and Fig. 4(i), we compare the effects of the variations of the virtual inertia from the reference value $\boldsymbol{M}_A = 4\boldsymbol{I}_3$ [Kg], with a decreased mass $\boldsymbol{M}_A = 2\boldsymbol{I}_3$ [Kg] and an increased one $\boldsymbol{M}_A = 6\boldsymbol{I}_3$ [Kg]. The aim is to analyze the performance of the system when high dynamics assignments are requested. In the examined cases, results show the impossibility for the system to satisfactorily shape the inertia, i.e., to track the ideal acceleration output corresponding to different virtual inertia. Several plausible reasons can be given. A good tracking of the virtual mass
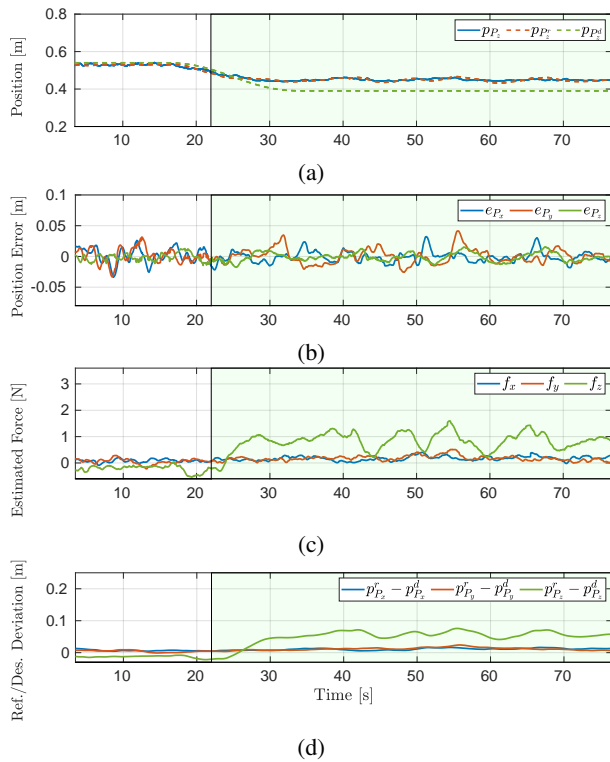
Fig. 5: Unexpected-collision interaction: 5(a) vertical actual platform position $\boldsymbol{p}_P$ in solid lines, desired position $\boldsymbol{p}_P^d$ and admittance reference $\boldsymbol{p}_P^r$ in dashed lines. 5(b): position error $\boldsymbol{e}_P$. 5(c): forces applied to the platform before and throughout the collision. 5(d): difference between the pre-planned trajectory and the references produced by the admittance filter.

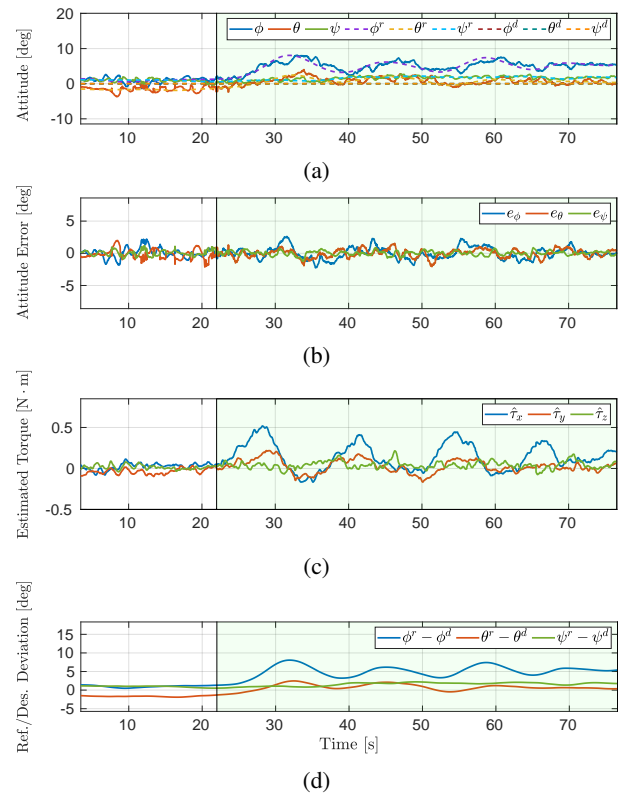Fig. 6: Unexpected-collision interaction: 6(a): actual platform orientation $\boldsymbol{\eta}_P$ in solid lines, desired orientation $\boldsymbol{\eta}_P^d$ and admittance reference $\boldsymbol{\eta}_P^r$ in dashed lines. 6(b): orientation error $\boldsymbol{e}_{\boldsymbol{\eta}_P}$. 6(c): torques applied to the platform before and throughout the collision. 6(d): difference between the pre-planned trajectory and the references produced by the admittance filter.

requires a very precise and theoretically instantaneous control of the thrust, which is impossible in our setup. In fact, the thrust is indirectly controlled through the rotor speeds, which are also subject to their first-order dynamics. On the other hand, the developed IKC controller is designed for tracking velocities rather than accelerations, and in general, the controller is purely based on feedback and it lacks the proper feed-forward term that is required to compensate for the inertial dynamics. A precise knowledge of such a term is indeed very difficult to attain in practice.

2) Unexpected-collision interaction: This experiment is designed to test the capability of the proposed aerial manipulation system to stably react to unexpected collisions and to adapt its behavior to such interaction. Additionally, the experiments also test the capabilities of the three aerial vehicles to maintain the cables' tightness at steady-state despite the contacts. To this end, a surface is placed in the middle of the arena, obstructing the way to the platform. The center of the surface is positioned at $[-1.55\ 0\ 0.50][\mathrm{m}]$ and its inclination about $\boldsymbol{x}_W$ is $8\ [\mathrm{deg}]$ (see Fig. 3(c)). The admittance parameters have been set as follows*: $\boldsymbol{K}_{A\boldsymbol{p}} = 15\boldsymbol{I}_3\ [\mathrm{N/m}]$ $\boldsymbol{D}_{A\boldsymbol{p}} = 50\boldsymbol{I}_3\ [\mathrm{Ns/m}]$, $\boldsymbol{K}_{A\boldsymbol{\eta}} = 2\boldsymbol{I}_3\ [\mathrm{N/rad}]$, $\boldsymbol{D}_{A\boldsymbol{\eta}} = 14\boldsymbol{I}_3\ [\mathrm{Ns/rad}]$, $\boldsymbol{M}_{A\boldsymbol{p}} = 2\boldsymbol{I}_3\ [\mathrm{Kg}]$ and $\boldsymbol{M}_{A\boldsymbol{\eta}} = 20\boldsymbol{I}_3\ [\mathrm{Kgm}^2]$. The experiment starts with the platform positioned at $\boldsymbol{p}_P =$

---

*The subscripts $\boldsymbol{p}$ and $\boldsymbol{\eta}$ refers to the gains in position and orientation respectively

$[-1.55\ 0\ -0.55][\mathrm{m}]$, followed by a descending phase toward $\boldsymbol{p}_P^d = [-1.55\ 0\ -0.43][\mathrm{m}]$. On its way, the platform collides with the surface.

Figures 5 and 6 present the crucial phases of the experiments. The area in which contacts occur has been highlighted in green. Fig. 5(a) shows the z components of the platform position, the desired trajectory, and the reference generated by the admittance filter. It can be appreciated how the admittance filter lets the reference deviate from the desired trajectory during the contact phase, thus indirectly keeping the pushing force limited in the direction of motion. In Fig. 5(b), we illustrate the position error $\boldsymbol{e}_P = \boldsymbol{p}_P^r - \boldsymbol{p}_P$ between the reference trajectory and the actual position of the robot. The norm $||\boldsymbol{e}_P||$ stays bounded around ± 4 [cm] in position during the experiment assuring, in such a way, a reliable position tracking for the task under exam. With Fig. 5(c), we show the first three components of $\hat{\boldsymbol{w}}_e$, namely the forces resulting from the external wrench estimation. In this graph, the contact, happening at $140[\mathrm{s}]$, is fully recognizable in f_z, as expected.

Figures 6(a) and 6(b) present similar plots for the orientation coordinates. The desired orientation changes from $\boldsymbol{\eta}_P = [0\ 0\ 0][\mathrm{deg}]$ to $\boldsymbol{\eta}_P \approx [-8\ 0\ 0][\mathrm{deg}]$ as a consequence of a non-zero estimated torque. In this variation, the norm of the orientation error $||\boldsymbol{e}_{\boldsymbol{\eta}_P}||$ holds at 2 [deg] which therefore allows to affirm that a reliable orientation tracking has been
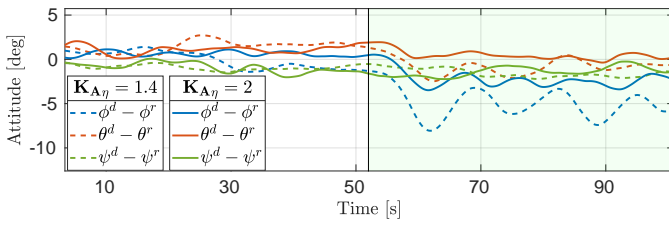
Fig. 7: The effect of changing the rotational stiffness about $\boldsymbol{x}_W$ between two experiments.

achieved despite the already discussed delay introduced by the wrench observer. The estimated torque experienced by the platform is shown in Fig. 6(c), and the orientation error between the pre-planned trajectory and the trajectory produced by the admittance filter is presented in Fig. 6(d). Similarly to the translation case, during the contact phase, the multi-robot system is capable of adapting the platform orientation with considerable accuracy.

The experiment has been repeated to show the effect of a different gain choice on the platform rotational compliance about $\boldsymbol{x}_W$. In particular, the gain has been lowered to $\boldsymbol{K}_{A\boldsymbol{\eta}} = \mathrm{diag}(1.4, 2, 2)$ [N/rad]. The aim is to obtain a more compliant behavior. Fig. 7 shows the difference between the two experiments. The previous one, characterized by a higher stiffness gain, is depicted in dotted lines. The last one is in dashed lines. As can be seen from the higher deviation between the desired and the reference trajectory in roll ($\phi^d - \phi^r$), the platform reaches a more compliant behavior when the stiffness gain is lower. Such a choice allows the platform to lean completely against the tilted surface. The effect of a different gain choice on the platform rotational compliance about $\boldsymbol{z}_W$ has also been evaluated, leading to similar conclusions. The interested reader is referred to the attached multimedia material to appreciate the behavior of the system in action.

V. CONCLUSIONS

We have addressed the challenging problem of controlling a complex cable-based aerial multi-robot manipulator while performing tasks in physical interaction with the environment. Our work shows that the problem can be solved using a suitable control architecture that combines algorithms at different levels. We have also shown that the approach is effective and reliable despite the absence of dedicated force/torque sensors, thanks to the implementation of a state-of-the-art wrench observer adapted to the *Fly-Crane*, our cable-based aerial multi-robot manipulator.

However, the method presents some limitations here summarized. First of all, the system has not been examined when collisions could demand agile moves far from quasi-static motions. Besides, the cable tautness has been only guaranteed at steady-state in the presented experiments. In the future, we intend to evaluate the system performances in the other two identified classes of interactions (i.e. Expected collisions and Active interchanges). Moreover, we plan to extend the capabilities of the proposed control approach to perform outdoor experiments. Less accurate robot localization

in outdoor conditions, as well as wind disturbances, will represent additional difficulties to be faced for the validation of control methods in real-world conditions. Finally, we intend to demonstrate the performances of our control framework in dealing with several tasks involving physical interactions such as pick-and-place manipulation or structure assembly in outdoor scenarios.

REFERENCES

[1] A. Ollero, M. Tognon, A. Suarez, D. J. Lee, and A. Franchi, "Past, present, and future of aerial robotic manipulators," *IEEE Trans. on Robotics*, vol. 38, no. 1, pp. 626–645, 2021.

[2] I. Palunko, P. Cruz, and R. Fierro, "Agile load transportation: Safe and efficient load manipulation with aerial robots," *IEEE Robotics & Automation Magazine*, vol. 19, no. 3, pp. 69–79, 2012.

[3] M. Tognon and A. Franchi, *Theory and Applications for Control of Aerial Robots in Physical Interaction Through Tethers*, ser. Tracts in Advanced Robotics.   Springer, 2020.

[4] Y. H. Tan, S. Lai, K. Wang, and B. Chen, "Cooperative control of multiple unmanned aerial systems for heavy duty carrying," *Annual Reviews in Control*, vol. 46, pp. 44–57, 2018.

[5] K. Sreenath and V. Kumar, "Dynamics, control and planning for co-operative manipulation of payloads suspended by cables from multiple quadrotor robots," in *Robotics: Science and Systems*, Berlin, Germany, June 2013.

[6] D. Prattichizzo and J. C. Trinkle, "Grasping," in *Springer Handbook of Robotics*, B. Siciliano and O. Khatib, Eds.   Springer, 2008, pp. 671–700.

[7] M. Manubens, D. Devaurs, L. Ros, and J. Cortés, "Motion planning for 6-D manipulation with aerial towed-cable systems," in *2013 Robotics: Science and Systems*, Berlin, Germany, May 2013.

[8] D. Sanalitro, H. J. Savino, M. Tognon, J. Cortés, and A. Franchi, "Full-pose manipulation control of a cable-suspended load with multiple UAVs under uncertainties," *IEEE Robotics and Automation Letters*, vol. 5, no. 2, pp. 2185–2191, 2020.

[9] A. Petitti, D. Sanalitro, M. Tognon, A. Milella, J. Cortés, and A. Franchi, "Inertial estimation and energy-efficient control of a cable-suspended load with a team of UAVs," in *2020 Int. Conf. on Unmanned Aircraft Systems*, Athens, Greece, Sep. 2020.

[10] S. Haddadin, A. De Luca, and A. Albu-Schffer, "Robot collisions: A survey on detection, isolation, and identification," *IEEE Transactions on Robotics*, vol. 33, no. 6, pp. 1292–1312, 2017.

[11] G. Nava, Q. Sablé, M. Tognon, D. Pucci, and A. Franchi, "Direct force feedback control and online multi-task optimization for aerial manipulators," *IEEE Robotics and Automation Letters*, vol. 5, no. 2, pp. 331–338, 2020.

[12] X. Meng, Y. He, Q. Li, F. Gu, L. Yang, T. Yan, and J. Han, "Contact force control of an aerial manipulator in pressing an emergency switch process," in *2018 IEEE/RSJ International Conference on Intelligent Robots and Systems (IROS)*, 2018, pp. 2107–2113.

[13] M. Ryll, G. Muscio, F. Pierri, E. Cataldi, G. Antonelli, F. Caccavale, D. Bicego, and A. Franchi, "6D interaction control with aerial robots: The flying end-effector paradigm," *The International Journal of Robotics Research*, vol. 38, no. 9, pp. 1045–1062, 2019.

[14] M. Tognon, C. Gabellieri, L. Pallottino, and A. Franchi, "Aerial co-manipulation with cables: The role of internal force for equilibria, stability, and passivity," *IEEE Robotics and Automation Letters, Special Issue on Aerial Manipulation*, vol. 3, no. 3, pp. 2577 – 2583, 2018.

[15] H. N. Nguyen, S. Park, J. Park, and D. Lee, "A novel robotic platform for aerial manipulation using quadrotors as rotating thrust generators," *IEEE Trans. on Robotics*, vol. 34, no. 2, pp. 353–369, 2018.

[16] A. De Luca and R. Mattone, "Sensorless robot collision detection and hybrid force/motion control," in *2005 IEEE Int. Conf. on Robotics and Automation*, Barcelona, Spain, Apr. 2005, pp. 999–1004.

[17] L. Villani and J. De Schutter, "Force control," in *Springer handbook of robotics*.   Springer, 2016, pp. 195–220.

[18] A. Franchi and A. Mallet, "Adaptive closed-loop speed control of BLDC motors with applications to multi-rotor aerial vehicles," in *2017 IEEE Int. Conf. on Robotics and Automation*, Singapore, May 2017, pp. 5203–5208.

[19] T. Lee, M. Leoky, and N. H. McClamroch, "Geometric tracking control of a quadrotor UAV on SE(3)," in *49th IEEE Conf. on Decision and Control*, Atlanta, GA, Dec. 2010, pp. 5420–5425.